Thermodynamic Stacking Fault Energy, Chemical Composition, and Microstructure Relationship in High-Manganese Steels

GIOVANI GONÇALVES RIBAMAR, TATHIANE CAMINHA ANDRADE, HÉLIO CORDEIRO DE MIRANDA, and HAMILTON FERREIRA GOMES DE ABREU

Stacking fault energy (SFE) is related to activating complex high strength and ductility mechanisms such as transformation-induced plasticity and twinning-induced plasticity effects. This type of energy can be estimated by many different methods and its importance is in its ability to predict microstructure and phase transformation behavior when the material is submitted to stress/strain. In order to study the SFE, chemical composition, and microstructure relationships, eleven different welding parameters were chosen to obtain a large range of dilution levels. A new tubular wire electrode of high-manganese steel (21 wt pct Mn) was used as the consumable and an SAE 1012 steel plate (0.6 wt pct Mn) as the base metal in a flux-cored arc welding process. These welding parameters were related to the phases formed and phase transformation behavior in the fusion zone. The SFE of the austenite phase was calculated using a thermodynamic model. The welding parameters produced SFE values in the range of -5 to 7 mJ/m^2. ϵ-martensite and austenite were observed in all samples, but α'-martensite was only found in those that presented negative SFE values, $i.e.$, those with lower Mn content. Chemical Gibbs Free energy was the component with the most influence on the SFE. Nanoindentation detected the phase transformations during hardness testing for the medium and low dilution levels used, while the high dilution levels presented the highest hardness and modulus of elasticity values, and the lowest elastic and plastic deformation values. The results provide an improved method to develop high-manganese steels with microstructure control through welding parameters.

I. INTRODUCTION

HADFIELD steels have elevated Mn levels. These steels have high wear resistance due to their austenite to martensite ($\gamma \rightarrow \alpha'$) transformation when submitted to stress/strain.[1,2] Currently, steels with manganese content higher than 20 wt pct have been produced with an excellent combination of high strength and ductility.[3–5] They have been classified in terms of their plasticity-enhancing mechanisms,[6] where twinning-induced plasticity (TWIP)[7–9] and transformation-induced plasticity (TRIP)[10–12] have been designated to those steels that present twin and martensite formation, respectively, when submitted to a stress/strain. In addition, the relationship between mechanical behavior and stacking fault energy (SFE) that austenite presents at some temperatures and compositions has been published.[7,13,14]

A stacking fault (SF) in the face-centered cubic (FCC) structure is a bi-dimensional fault formed between partial dislocations when normal stacking sequence of the (111) plane is disturbed.[7] This change in stacking sequence produces an interface separating two regions in the matrix and is related to interface energy. Otte[15] and Smallman and Westmacott[16] studied the influence of manganese and chromium content in the presence of SFs and the influence of elevated temperature deformation on the probability of faulting. These authors reached the conclusion that these alloying elements increase the susceptibility of FCC austenite to faulting,

GIOVANI GONÇALVES RIBAMAR is with the Universidade de São Paulo, Escola Politécnica, Departamento de Engenharia Metalúrgica e de, Materiais, Av. Professor Mello Moraes, 2463, São Paulo, CEP: 05508-030, Brazil. Contact e-mail: giovanigoncalvesr@gmail.com TATHIANE CAMINHA ANDRADE, HÉLIO CORDEIRO DE MIRANDA, and HAMILTON FERREIRA GOMES DE ABREU are with the Universidade Federal do Ceará, Departamento de Engenharia Metalúrgica e de Materiais, Campus do Pici, Bloco 729, Ceará, CEP 60.440-554, Brazil.

as well as decrease the deformation temperature. The SFE can be determined by transmission electron microscopy (TEM)[17] and X-ray diffraction.[18] In addition, SFE has been calculated by Ab-initio[19,20] and thermodynamic models,[7,14] among others. The latter was used to determine the SFE for all welding samples in this study. These methods of determining the SFE through calculations and thus the ability to predict the microstructure and mechanical behavior from the SFE value make the SFE an excellent tool to design materials with specific properties.

In general, high-manganese steel with SFE close to 0 mJ/m² has been reported to present ϵ-martensite after a rapid cooling from a γ phase field. However, an increase in SFE until approximately 15 mJ/m² presents ϵ-martensite and twins when the material is submitted to a deformation, which is characteristic of a TRIP steel.[6,7,13] Above approximately 15 mJ/m², twins are formed in austenite when the material is submitted to a stress/strain, which is characteristic of TWIP steel.[21,22] However, as Remy and Pineau[22] and Allain et al.[21] have shown, this relationship between the SFE range and the material behavior depends on the alloying elements. Lee et al.[23] found that for low SFE, α'-martensite is present after the formation of ϵ-martensite. It is important to mention that both ϵ and α'-martensite are metastable and are not found on an equilibrium phase diagram. Depending on the alloy content, these phases can be formed after rapid cooling from a γ phase; however, the α' phase can present different morphologies.[24] Hwang, who studied high-manganese steels with cooper and aluminum additions, obtained alloys with SFEs greater than 15 mJ/m² and no ϵ- or α'-martensite.[25] However, high-carbon steels with such SFE values present the formation of ϵ- and α'-martensite, as well as twins when submitted to stress/strain.[26]

In this study, the influence of the chemical composition on the microstructure and phase transformation behavior was evaluated using the different welding dilutions between two steels with different Mn contents: a new high-manganese welding wire of composition Fe-21Mn-3.8Ni-0.17C (wt pct) and a low manganese SAE 1012 steel of composition Fe-0.6Mn-0.12C (wt pct). The different manganese contents of the welding deposits were determined and related to the SFE values. This is a new approach in the microstructure-stacking fault energy relationship studies. Eleven alloys were obtained, varying the dilution levels from 7.6 to 41.0 pct, producing a manganese composition from 12 to 20 wt pct. The microstructure was observed using scanning electron microscopy (SEM) and electron backscatter diffraction (EBSD). The phase transformation behavior was analyzed through nanoindentation tests that also gave Young's modulus. These measurements enabled the dilution levels, the SFEs, the microstructures, and the physical properties to be related to the high-manganese tubular wire electrode used. The SFE analyses, through individual Gibbs free energy components, were carried out and the results were extended to other high-manganese steels presented in the literature. This study is important for the study of high-manganese steels, as it enables the prediction of weld microstructures through SFE calculation of welding deposits produced using different dilution levels.

II. METHODS

A. Stacking Fault Energy Calculations

The SFE was calculated for the Fe-Mn-C-Ni-Si-Cr system over a wide range of compositions at room temperature (27 °C) based on the thermodynamic model proposed by Olson and Cohen[27] and later modified by other authors. Besides the existence of many papers with SFE equations calculated by the thermodynamic model, the texts can be confusing with the modifications and assumptions that each author has made. Thus, the present work shows all equations and parameters used for the SFE calculations.

All ΔG variables shown here are in J/mol unit.

When an SF is introduced into a perfect crystal, there will be a change in the Gibbs energy, ΔG. According to Curtze and Kuokkala,[7] this change in ΔG must be the same for both the interface and volume approach:

$$\Delta G_{if} = \Delta G_{vol} \quad [1]$$

Curtze and Kuokkala[7] showed how to develop Eq. [1] to achieve the SFE equation, as shown in Eq. [2]:

$$SFE = 2\rho \Delta G^{\gamma \to \epsilon} + 2\sigma^{\gamma/\epsilon} \quad [2]$$

where ρ is the molar surface density for the $\{111\}_\gamma$ closed packed planes (mol/m²), $\Delta G^{\gamma \to \epsilon}$ is the molar Gibbs energy of the $\gamma \to \epsilon$ phase transformation and $\sigma^{\gamma/\epsilon}$ is the energy per surface unit of the $\{111\}$ interface between the γ and ϵ phase boundary (J/m²). According to Allain et al.,[21] $\sigma = 9$ mJ/m² for steels with a similar chemical composition. The molar surface energy can be calculated by:

$$\rho = \frac{4}{\sqrt{3}} \frac{1}{a^2 N} \quad [3]$$

where a is the lattice parameter of austenite (m) and N is Avogadro's constant. $\Delta G^{\gamma \to \epsilon}$ can be calculated by:

$$\Delta G^{\gamma \to \epsilon} = \Delta G_{che}^{\gamma \to \epsilon} + \Delta G_{mg}^{\gamma \to \epsilon} + \Delta G_{seg}^{\gamma \to \epsilon} \quad [4]$$

where $\Delta G_{che}^{\gamma \to \epsilon}$ and $\Delta G_{mg}^{\gamma \to \epsilon}$ are the molar thermochemical and magnetic Gibbs energy components, respectively. $\Delta G_{seg}^{\gamma \to \epsilon}$ is the free energy component due to the Suzuki effect between γ and ϵ, neglected here since its value is very low at room temperature.[28] $\Delta G_{che}^{\gamma \to \epsilon}$ can be written as the sum of two terms:

$$\Delta G_{che}^{\gamma \to \epsilon} = \sum_i \chi_i \Delta G_i^{\gamma \to \epsilon} + \sum_i \chi_i \chi_j \Omega_{ij}^{\gamma \to \epsilon} \quad [5]$$

where χ_i is the molar fraction of the pure alloying elements and $\Delta G_i^{\gamma \to \epsilon}$ is the chemical contributions to the change in Gibbs energy due to χ_i. $\Omega_{ij}^{\gamma \to \epsilon}$ refers to the excess free energies of the interaction between the pure

elements (J/mol). $\Delta G_i^{\gamma\to\epsilon}$ can be calculated as shown by Dinsdale,[29] using Equation (6):

$$\Delta G_i^{\gamma\to\epsilon} = G_i^\epsilon - G_i^\gamma \qquad [6]$$

where G_i^ϵ and G_i^γ are the molar Gibbs energy of the pure elements in the ϵ and γ phases, respectively. The Gibbs energy is represented as a power series and the equations for G_i^ϵ and G_i^γ can be found in Dinsdale.[29] Equation [7] represents the function for G_i^ϕ:

$$G_i^\phi = a + bT + cT\ln T + \sum_{i,n} d_i T^n \qquad [7]$$

where a, b, c, and d_i are coefficients, T is the temperature in Kelvin, and n represents a set of integers, typically taking the values of 2, 3, and -1.[29] The excess free energy of a multicomponent system can be calculated by the sum of the excess free energy associated with the interaction of the elements two by two.[30] Therefore, $\Omega_{ij}^{\gamma\to\epsilon}$ (the excess free energy of i and j interaction) can be calculated according to Eq. [8].[31]

$$\Omega_{ij}^{\gamma\to\epsilon} = \left({}^0L^\epsilon - {}^0L^\gamma\right) + \left({}^1L^\epsilon - {}^1L^\gamma\right)\left(\chi_i - \chi_j\right) \qquad [8]$$

where ${}^0L^\epsilon$ is a linear function of the temperature and ${}^1L^\epsilon$ is a constant. Table I shows all functions that describe the chemical change contribution of the Gibbs free energy upon the $\gamma \to \epsilon$ phase transformation.

The magnetic contribution, $\Delta G_{\mathrm{mg}}^{\gamma\to\epsilon}$, in Eq. [4] can be calculated by:

$$\Delta G_{\mathrm{mg}}^{\gamma\to\epsilon} = \Delta G_{\mathrm{mg}}^\epsilon - \Delta G_{\mathrm{mg}}^\gamma \qquad [9]$$

where $\Delta G_{\mathrm{mg}}^\epsilon$ and $\Delta G_{\mathrm{mg}}^\gamma$ are the magnetic contributions of the ϵ and γ phases, respectively, calculated according to Inden[38]:

$$G_{\mathrm{mg}}^\Phi = RT\ln(\beta^\Phi + 1)f^\Phi(\tau^\Phi) \qquad [10]$$

where R is the gas constant in J/K mol, T is the temperature (K), β^Φ is the magnetic moment divided by the Bohr magneton μ_B, and $f^\Phi(\tau^\Phi)$ is a polynomial function of the Néel temperature.[7] β^Φ is calculated by:

$$\beta^\gamma = \chi_{\mathrm{Fe}}\beta_{\mathrm{Fe}} + \chi_{\mathrm{Mn}}\beta_{\mathrm{Mn}} + \chi_{\mathrm{Ni}}\beta_{\mathrm{Ni}} - \chi_{\mathrm{Cr}}\beta_{\mathrm{Cr}}$$
$$- \chi_{\mathrm{Fe}}\chi_{\mathrm{Mn}}\beta_{\mathrm{FeMn}} - \chi_{\mathrm{C}}\beta_{\mathrm{C}} \qquad [11]$$

$$\beta^\epsilon = \chi_{\mathrm{Mn}}\beta_{\mathrm{Mn}} - \chi_{\mathrm{C}}\beta_{\mathrm{C}} \qquad [12]$$

τ^Φ can be calculated using Eq. [13]:

$$\tau^\Phi = \frac{T}{T_{N\acute{e}el}^\Phi} \qquad [13]$$

where $T_{N\acute{e}el}^\Phi$ (K) for the γ and α phases are given by the following equations:

$$T_{N\acute{e}el}^\gamma = 10\chi_{\mathrm{Mn}}^3 - 898.4\chi_{\mathrm{Mn}}^2 + 1176\chi_{\mathrm{Mn}} - 1992\chi_{\mathrm{C}}$$
$$- 1272\chi_{\mathrm{Si}} - 661\chi_{\mathrm{Al}} - 170\chi_{\mathrm{Cr}} + 152.4 \qquad [14]$$

$$T_{N\acute{e}el}^\epsilon = 580\chi_{\mathrm{Mn}} \qquad [15]$$

$f^\Phi(\tau^\Phi)$ is related to a condition where for $\tau^\Phi \leq 1$:

$$f^\Phi(\tau^\Phi) = 1 - \frac{\left[\frac{79\tau^{-1}}{140p} + \frac{474}{497}\left(\frac{1}{p} - 1\right)\left(\frac{\tau^3}{6} + \frac{\tau^9}{135} + \frac{\tau^{15}}{600}\right)\right]}{D} \qquad [16]$$

and for $\tau^\Phi > 1$:

$$f^\Phi(\tau^\Phi) = -\frac{\left[\frac{\tau^{-5}}{10} + \frac{\tau^{-15}}{315} + \frac{\tau^{-25}}{1500}\right]}{D} \qquad [17]$$

According to Curtze and Kuokkala,[7] D can be calculated by:

$$D = \frac{518}{1125} + \frac{11692}{15975}\left(\frac{1}{p - 1}\right) \qquad [18]$$

Table I. Functions Describing the Gibbs Free Energy Chemical Change Contribution Upon $\gamma \to \epsilon$ Phase Transformation Showed in Eqs. [5] Through [8]

Parameter	Function (J/mol)	References
$\Delta G_{\mathrm{Fe}}^{\gamma\to\epsilon}$	$-2243.38 + 4.309T$	29
$\Delta G_{\mathrm{Mn}}^{\gamma\to\epsilon}$	$-1000 + 1.123T$	29
$\Delta G_{\mathrm{Ni}}^{\gamma\to\epsilon}$	$1046 + 1255T$	28
$\Delta G_{\mathrm{Cr}}^{\gamma\to\epsilon}$	$1370 - 0.163T$	28
$\Delta G_{\mathrm{Si}}^{\gamma\to\epsilon}$	$-560 - 8T$	32
$\Delta G_{\mathrm{Cu}}^{\gamma\to\epsilon}$	$600 + 0.2T$	29
$\Delta G_{\mathrm{Al}}^{\gamma\to\epsilon}$	$2800 + 5T$	32
$\Delta G_{\mathrm{C}}^{\gamma\to\epsilon}$	-22166	33,34
$\Omega_{\mathrm{FeMn}}^{\gamma\to\epsilon}$	$2873 + 717(\chi_{\mathrm{Fe}} - \chi_{\mathrm{Mn}})$	35
$\Omega_{\mathrm{FeC}}^{\gamma\to\epsilon}$	42500	36
$\Omega_{\mathrm{MnC}}^{\gamma\to\epsilon}$	26910	21
$\Omega_{\mathrm{FeAl}}^{\gamma\to\epsilon}$	3328	34
$\Omega_{\mathrm{FeSi}}^{\gamma\to\epsilon}$	$2850 + 3520(\chi_{\mathrm{Fe}} - \chi_{\mathrm{Mn}})$	32
$\Omega_{\mathrm{FeCr}}^{\gamma\to\epsilon}$	2095	37
$\Omega_{\mathrm{FeNi}}^{\gamma\to\epsilon}$	2095	37
$\Omega_{\mathrm{CrNi}}^{\gamma\to\epsilon}$	4190	37

Table II. Functions and Constants Describing the Gibbs Free Energy Magnetic Change Contribution Upon $\gamma \to \epsilon$ Phase Transformation Showed in Eqs. [10] Through [13] and [16] Through [18]

Parameters	Function/Constant	References
β_{Fe}	0.70	39
β_{Mn}	0.62	39
β_{Ni}	0.62	40
β_{Cr}	0.80	29
β_{FeMn}	0.64	32
β_{C}	4.00	32
p	0.28	7
a	3.6×10^{-10} m	
T	300 K	

All the constants for the magnetic contribution to the Gibbs energy are given in Table II.

B. *Welding Parameters*

The weld beads were made using the FCAW process with a high-manganese electrode on SAE 1012 steel plate using different welding parameters. The chemical composition of the consumable is given in Table III. Plates 20 cm in length and 10 cm in width were used as the base metal, providing approximately 16 cm long beads. The dilution levels were determined using a geometric method, which uses the areas of the base metal (A_{BM}) and filler metal (A_{FM}) composing the fusion zone, according to Eq. [19].[41] A sample with six layers of weld beads was made in order to achieve a sample with minimal influence of the base metal to determine the filler metal chemical composition. The filler and base metal chemical compositions were measured using a Shimadzu PDA 7000 Optical Emission Spectrometer. All the weld bead chemical compositions were determined by energy-dispersive spectroscopy *via* scanning electron microscopy (SEM-EDS) and the carbon content was calculated using Eq. [20].[42]

$$D = \frac{A_{BM}}{A_{BM} + A_{FM}} \quad [19]$$

$$C_{FZ}^{C} = DC_{textBM}^{C} + (1 - D)C_{textFM}^{C} \quad [20]$$

where C_{FZ}^{C}, C_{BM}^{C}, and C_{FM}^{C} are the carbon content in the fusion zone, base metal, and filler metal, respectively.

Different welding parameters were used to achieve a range of dilution levels. All welding parameters were made at constant tension while varying: current, filler metal feed rate, and welding speed, as shown in Table IV, and they are presented in order of the power used. Later in this study, the order will be reorganized by dilution level to make the correlation with the results clearer.

C. *Microstructural Characterization*

Sample preparation was carried out using standard metallography procedures, which involved grinding with silicon carbide papers down to grade 1200, followed by polishing with 3 and 1 μm diamond suspensions. Final polishing was carried out with colloidal silica. The samples were etched with a 10 pct Nital (10 pct Nitric Acid + 90 pct Alcohol) solution. For microstructural analyses, scanning electron microscopy (SEM), X-ray energy-dispersive spectroscopy (EDS), and electron

Table III. Base Metal and High-Manganese Electrode Chemical Compositions

	Mn	Ni	Cr	Si	C	Fe
PT-400HM	20.935	3.763	0.865	0.5805	0.17	bal.
SAE 1012	0.6	—	—	—	0.12	bal.

All values are in Wt Pct.

backscatter diffraction (EBSD) observations were carried out using an FEI-XL50 with a field emission gun at 20 kV. In the EBSD analysis, the specimen tilt angle was 70 °C with a 17 mm working distance and different step sizes.

Nanoindentation tests were carried out using a Triboindenter TI 950 (Hysitron Inc.) in the load control testing mode with a maximum load of 5 μN and a Berkovich type indenter. A matrix of 16 × 16 indentations was performed with a 10 μm spacing between indents in both the vertical and horizontal directions. All tests were made at room temperature, after surface polishing to 1 μm. The analyses for contact area estimation and hardness value calculations were conducted using the method proposed by Oviler and Pharr.[43]

III. RESULTS

This study used eleven dilution levels (Figure 1) that varied within the 7.6 to 41.0 pct range. Aside from some welding samples that presented similar dilution values, such as A2 and A3 or B9 and B10, different levels were achieved with different welding parameters. No welding sample presented a lack of fusion or undercutting, and the weld beads were homogeneous with a good surface finish. The beads were named in descending order of dilution level, from 1 to 11. Those which presented α'-martensite in the microstructure were identified with the letter "A" before the number and those which did not present it were identified with the letter "B" before the number, as shown in the x-label of Figure 1.

The chemical composition of the samples was measured using SEM-EDS and is shown in Table V. On analyzing the decrease in the dilution levels, there are two important elements that increase: Mn has the highest increase varying from 13.40 to 18.91 pct and the nickel varies from 2.26 to 3.42 pct. Since the SEM-EDS technique does not determine the carbon content accurately, it was obtained using Eq. [20], Table III, and Figure 1 data. DuPont and Marder[41] studied the linear correlation between calculated and measured dilution levels. Their results showed the possibility to obtain the carbon content in this work using the dilution level measured by a geometric method. Carbon did not present any significant influence due to the similar base metal and electrode carbon content, 0.12 and 0.17 wt pct, respectively. The other elements presented a small increase with the decrease of the dilution level.

Besides the composition that was measured in a large area of the fusion zone, the microsegregation that was possibly formed during the solidification of the fusion zone was also measured. Figure 2 shows map compositions for high (Figures 2(a) through (c)) and low (Figures 2(d) through (f)) dilution levels. These maps present one SEM image and one composition map for Fe and one for Mn per sample. The intensity in the map compositions shows the concentration of the element. In A3 weld, there are austenite and α'-martensite regions in which there are manganese poor areas localized where

Table IV. Processing Parameters Used to Fabricate Single Pass in all Conditions

Condition	Welding Parameters					
	Power (W)	Current (A)	Tension (V)	Welding Speed (cm/min)	Feed Rate (m/min)	Energy (kJ/mm)
A2	5100	150	34	30	7	1.0
A5	5890	190	31	30	8	1.2
B10	7480	220	34	15	10	3.0
B11	7480	220	34	22	10	2.0
A4	7480	220	34	30	10	1.5
A3	7480	220	34	45	10	1.0
B8	8840	260	34	30	16	1.8
A1	9200	230	40	45	12	1.2
A6	9724	286	34	45	20	1.3
B7	9758	287	34	30	20	2.0
B9	10,000	250	40	30	12	2.0
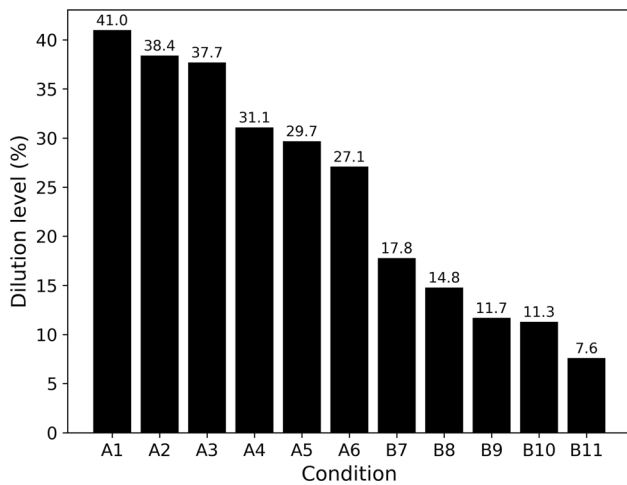
Fig. 1—Dilution level for each condition obtained by geometric method.

Table V. Chemical Composition of all Samples in Wt Pct

Condition	Mn	C	Ni	Si	Cr	Fe
A1	13.40	0.15	2.26	0.32	0.59	bal.
A2	13.57	0.15	2.32	0.29	0.54	bal.
A3	12.69	0.15	2.05	0.32	0.51	bal.
A4	14.69	0.15	2.66	0.51	0.59	bal.
A5	14.65	0.16	2.61	0.49	0.57	bal.
A6	15.95	0.16	2.76	0.36	0.61	bal.
B7	18.07	0.16	3.41	0.40	0.75	bal.
B8	17.63	0.16	3.30	0.59	0.76	bal.
B9	16.99	0.16	3.08	0.53	0.68	bal.
B10	18.71	0.16	3.49	0.50	0.82	bal.
B11	18.91	0.17	3.42	0.54	0.76	bal.

to A6. However, microsegregation was observed in all the welding samples, and the amount was dependent on the dendrite size.

Phase diagrams were constructed from the chemical compositions given in Table V using Thermocalc® thermodynamic software with the TCFE8 database. Figures 3(a) through (c) show phase diagrams for welding samples A1, A6, and B11, respectively. The equilibrium phases calculated were austenite, ferrite, M_7C_3, and $M_{23}C_6$. M_7C_3 and $M_{23}C_6$ are formed at low temperatures and were found in small amounts compared to the other phases. However, these carbides are not found in high-manganese steels due to the rapid cooling that they are submitted to from the austenite temperature range.[6,44,45] Ferrite presents a mass fraction of approximately 0.6 for the highest dilution level at temperatures close to 400 °C and decreases to approximately 0.4 at the lowest dilution level. Austenite is the only phase in equilibrium at temperatures higher than 600 °C, but this temperature decreases with decreasing dilution levels.

Figure 3(d) shows the austenite mass fraction for all welding samples. The austenite phase field increased with decreasing dilution levels due to the increase in γ stabilizers. The ferrite phase also is influenced by the addition of manganese and its phase field decreases with decreasing dilution levels. It is important to mention that ϵ- and α'-martensite phases are not in equilibrium phase diagrams because they are diffusionless phases and thus cannot be calculated using the Thermocalc®. The diagrams are mainly used to show austenite stability and any other phases that can be present, assuming a state of diffusion.

The thermodynamic SFE was calculated using Equation (2) and Table V at 27°C. Figure 4 shows the SFE values for all welding samples. Negative SFE values were obtained for six welding samples which were when SFE increased with decreasing dilution levels, with the exception of A3. Although the thermodynamic SFE might be calculated for a $\gamma \rightarrow \epsilon$ phase transformation where the chemical composition is taken from the austenite, in the present work, the compositions were taken from either γ, ϵ or α'. From welding samples A6 to

α'-martensite formed, and for B7 weld, there are also manganese-rich and -poor regions; however, α'-martensite was not found. This absence of manganese, and consequently, iron rich regions where α'-martensite had formed, was observed for all welding samples from A1
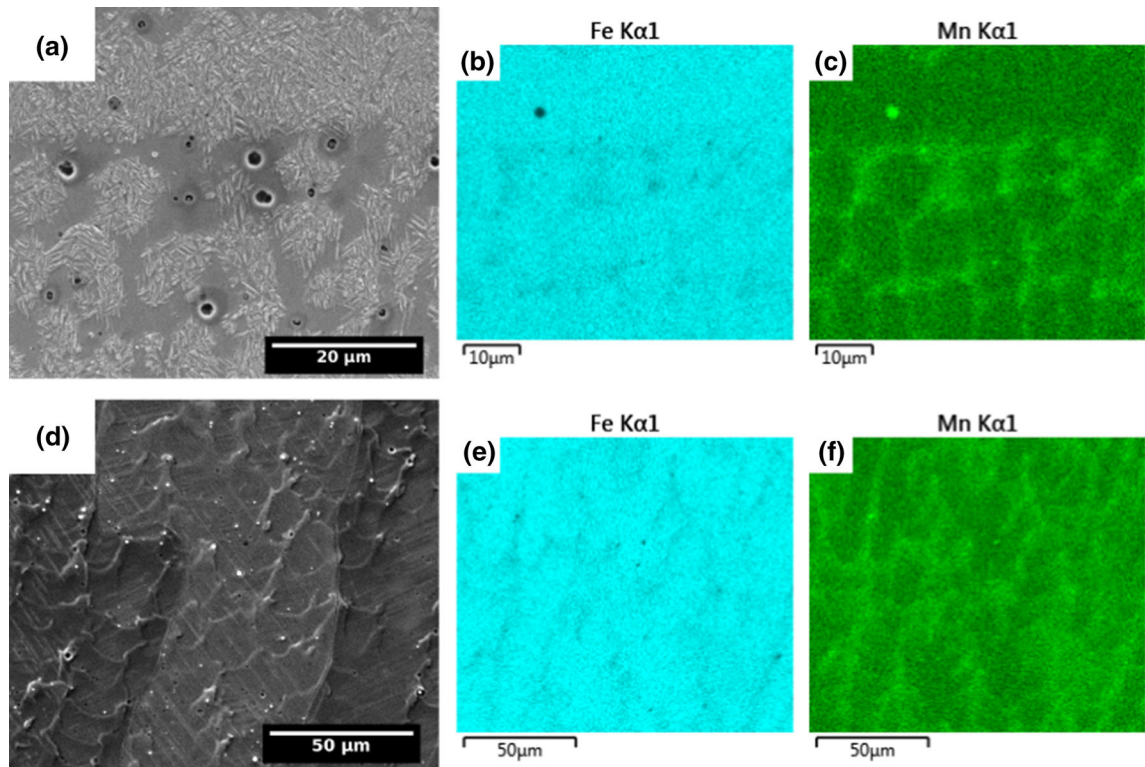
Fig. 2—SEM images and map compositions for a high (A3 weld) and a low (B7 weld) dilution level condition. (*a* to *c*) High dilution level. (*d* to *f*) Low dilution level. (*a*, *d*) SEM images of regions analyzed, while (*b*, *e*) and (*c*, *f*) iron and manganese composition map, respectively.

B7, there was a significant increase in the SFE value, and then, it reduced until B9 weld, after which SFE increased again to samples B10 and B11. Although the SFE values were calculated from an average composition measured by SEM-EDS, the microsegregation was examined and showed similar results to the phase-forming regions, *i.e.*, regions with a lower Mn content showed the α'-martensite phase, while those which displayed a high-Mn content did not show this phase.

SEM micrographs are presented in Figure 5. The three upper micrographs (Figures 5(a) through (c)) present two regions. One region are the α'-martensite laths. The other is related to a mixture of austenite and ϵ-martensite. Etching was not able to separate these two microstructures, but EBSD measurements were able to differentiate them. Increasing the dilution level decreased the presence of α'-martensite. α'-martensite was observed in the core of the dendrite; however, less α'-martensite was formed when there was a higher manganese content. Figures 5(d) through (f) did not show α'-martensite. Instead, the presence of twins in the structure was noted. They were identified as twins and not scratches because the twin orientation changes in the grain boundary, as shown in Figure 5(e). Dendrites, which are a feature of cast structures, were present in all micrographs.

Nanoindentation measurements were carried out for high (A1), medium (A6), and low (B11) dilution levels. Figure 6(a) shows one measurement for each level. There are pop-in indications for weld samples A6 and B11. Several works reported the presence of a pop-in during nanoindentation in austenite as a martensite transformation, either into ϵ'- or α-martensite.[46–50] Ahn *et al.* explained this behavior as resulting from geometrical softening due to the selection of a favorable martensite variant based on the mechanical interaction energy between the externally applied stress and lattice deformation during nanoindentation.[50] Therefore, the authors strongly believe that the pop-ins presented in Figure 6(a) correspond to a martensite transformation. In this work, they correspond to the $\gamma \rightarrow \epsilon \rightarrow \alpha'$ transformation, where the first, second, or even the two transformations can occur. A1 weld shows little deformation and low recovery in the unload step compared to the other welding beads. While A1 weld did not show a pop-in, B11 showed the highest occurrence of phase transformations during the test. This lack of a pop-in in A1 may be because no measures were made in the γ/ϵ phase region, which is much smaller than the α'-martensite phase regions.

In order to quantify and analyze the nanoindentation tests in terms of the mechanical properties, as shown by Oliver and Pharr,[43] Figure 6(b) was plotted. The A1
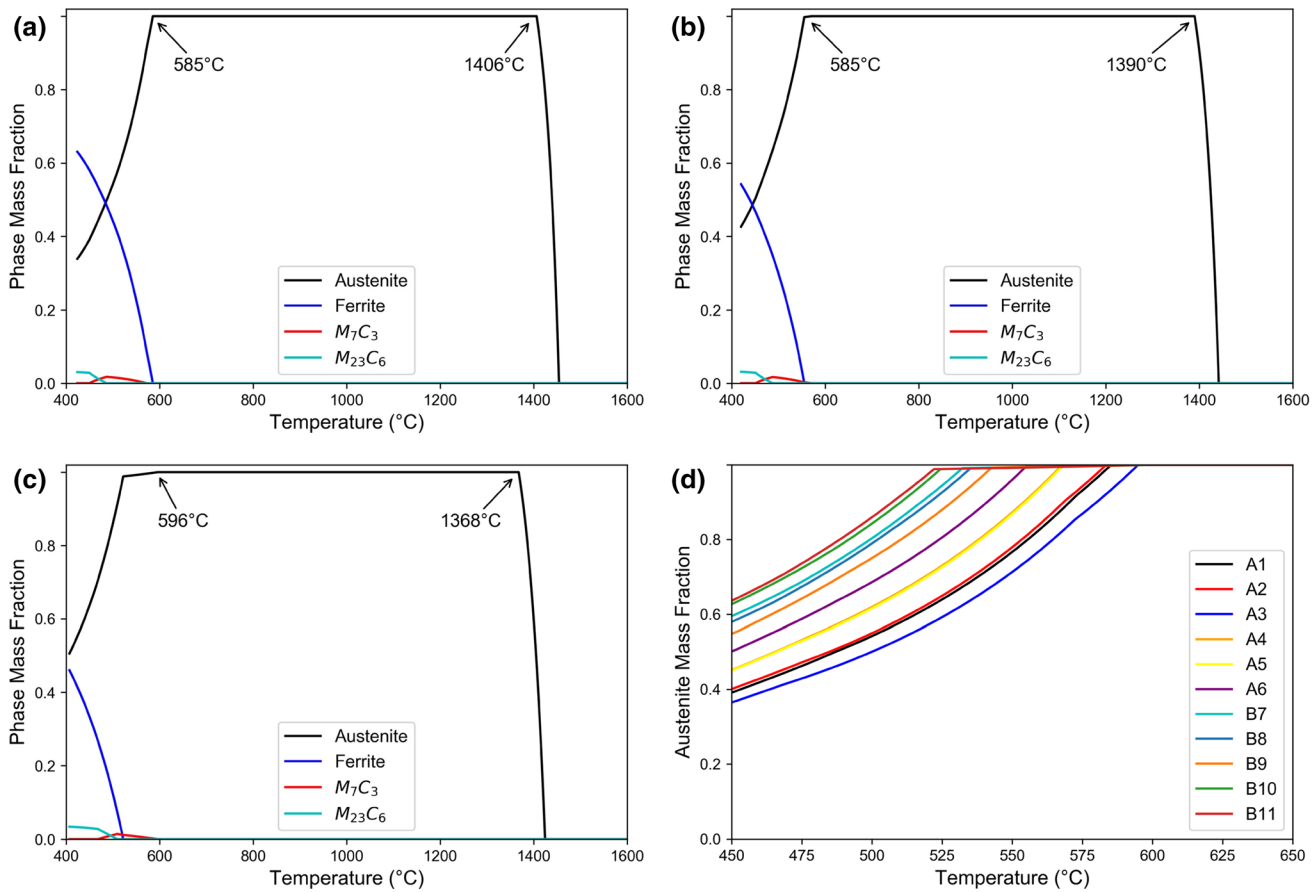
Fig. 3—(a to c) Phase mass fraction diagram for A1, A6, and B11 samples, respectively. (d) Austenite mass fraction diagram for all conditions.
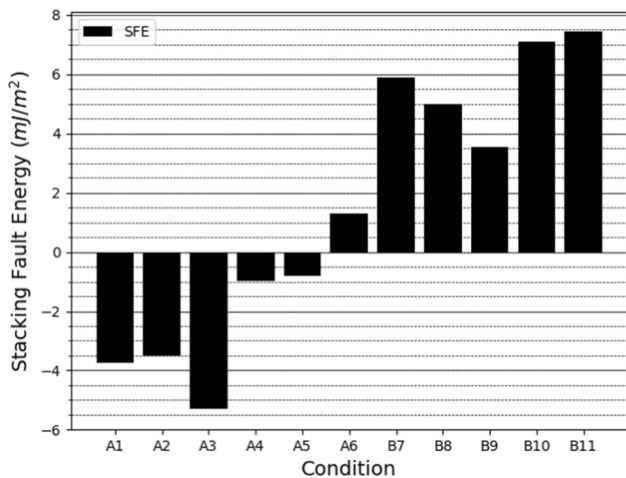

Fig. 4—Stacking fault energy for each sample obtained by thermodynamic calculations.

weld showed an elastic modulus of 177 GPa and a hardness value of 6.67 GPa. A decrease in the dilution levels decreased both the hardness and elastic modulus. B11 weld presents an elastic modulus 33 pct of the A1 value, while the hardness value is almost 72 pct of the A1 value. Referring to other works which studied the mechanical properties of high-manganese steels,[6,51,52]

the increase in Mn content changes the mechanical behavior through austenite stability.

EBSD measurements can give crystallographic orientation information and phase identification, enabling the correct characterization allied to other techniques and making it possible to determine the crystallographic orientation of the phases present. Figure 7 shows the EBSD results measured in the same three welding beads used in the nanoindentation tests. Figures 7(a) through (c) show the inverse pole figure maps for samples A1, A6, and B11, respectively. α'-martensite is presented as laths, refining the structure, while ϵ-martensite has formed into γ grains with a specific orientation, as shown in Figure 7(c). α'- and ϵ-martensite, as well as austenite, were observed in A6 weld.

Figure 7(e) shows α'-martensite formed in straight lines until the grain boundary. This α' can be seen in many crystallographic orientations. No α'-martensite was observed in B11 weld aside from a point in the upper right of Figure 7(g). However, ϵ-martensite and austenite were observed in all samples, while α' was only noted in samples A1 and A6. At the high dilution level, the fraction of ϵ-martensite obtained by EBSD was approximately 56 pct, with 21 and 23 pct for α' and γ, respectively. In A6, there were greater volume decreases austenite (42 pct) and ϵ-martensite (34 pct). At the lowest dilution level, 90 pct austenite was present with almost 10 pct ϵ-martensite. These results suggest that the
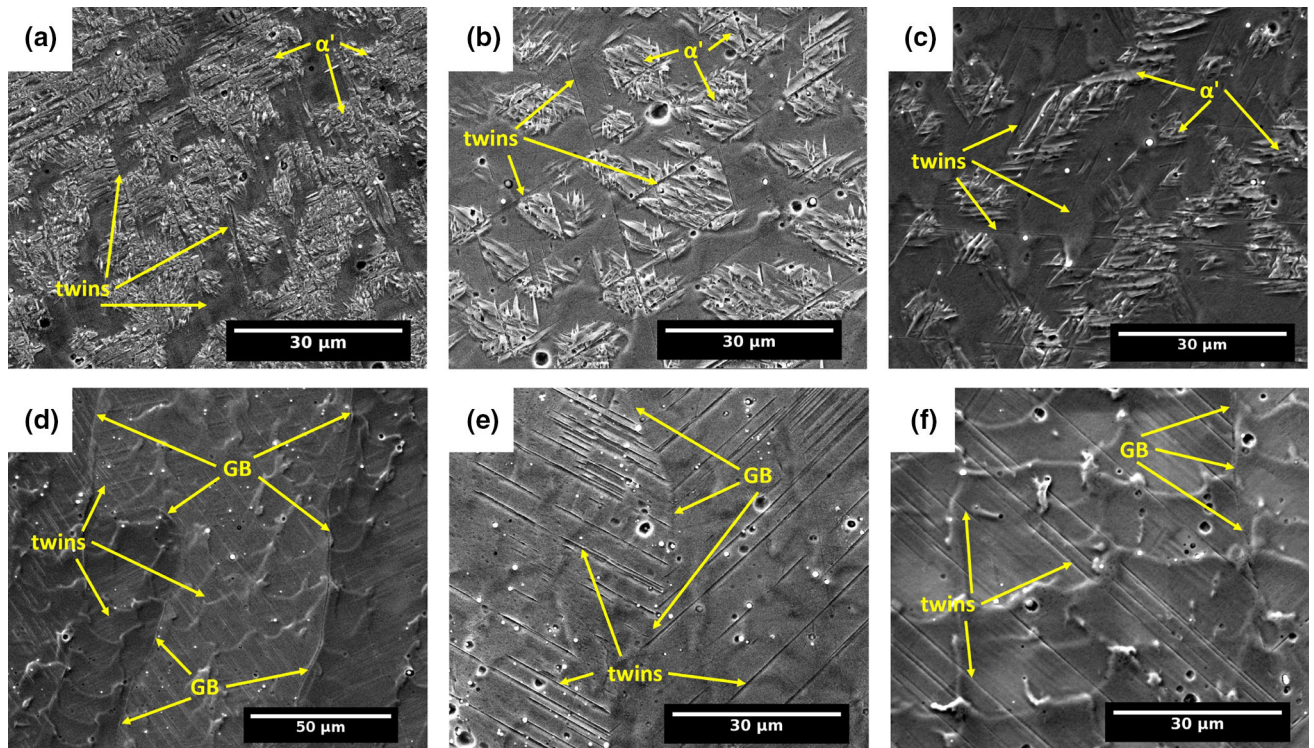
Fig. 5—Electronic micrographs from fusion zone of conditions (*a*) A1, (*b*) A4, (*c*) A6, (*d*) B7, (*e*) B9, and (*f*) B11. GB: grain boundaries. α′: α′-martensite.
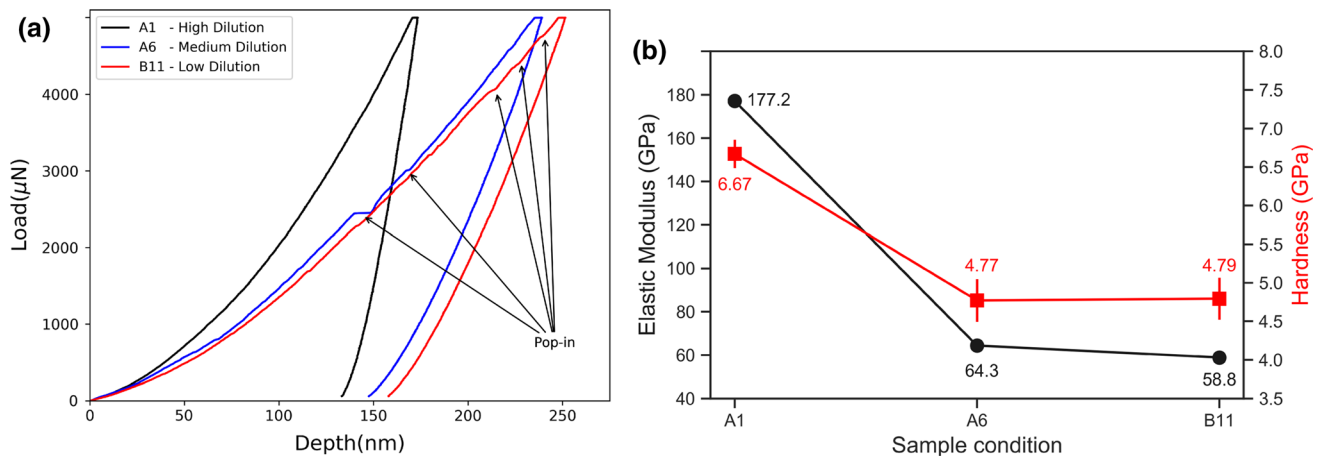

Fig. 6—(*a*) Indentation test for one condition at: high, medium, and low dilution. The arrows are indications of phase transformation during the test. (*b*) Hardness and Elastic modulus of samples at high, medium, and low dilution. The standard deviation bar of elastic modulus data is smaller than the markers.

dilution level could stabilize the austenite phase through manganese and nickel enrichment.

IV. DISCUSSION

A. *Dilution Levels and Chemical Composition*

Eleven different alloys were formed at the fusion zone, using SAE 1012 steel as the base metal and PT-400HM as the filler metal. By varying the weld parameters, dilution levels as high as 41 pct and as low as 7.6 pct

(Figure 1) were created. In general, when the feed rate was high, the dilution level was also high. Also, when a power of 7480 W was applied there was an increase in the dilution levels with a decrease in welding speed (Table IV). The influence of both the feed rate and welding speed on the dilution level can be explained by the protection that the weld pool can provide to the base metal, preventing the arc welding from melting more of the base metal. With a decreasing welding speed, the arc remains in the melt pool longer, allowing more filler metal to be deposited and increasing the barrier between
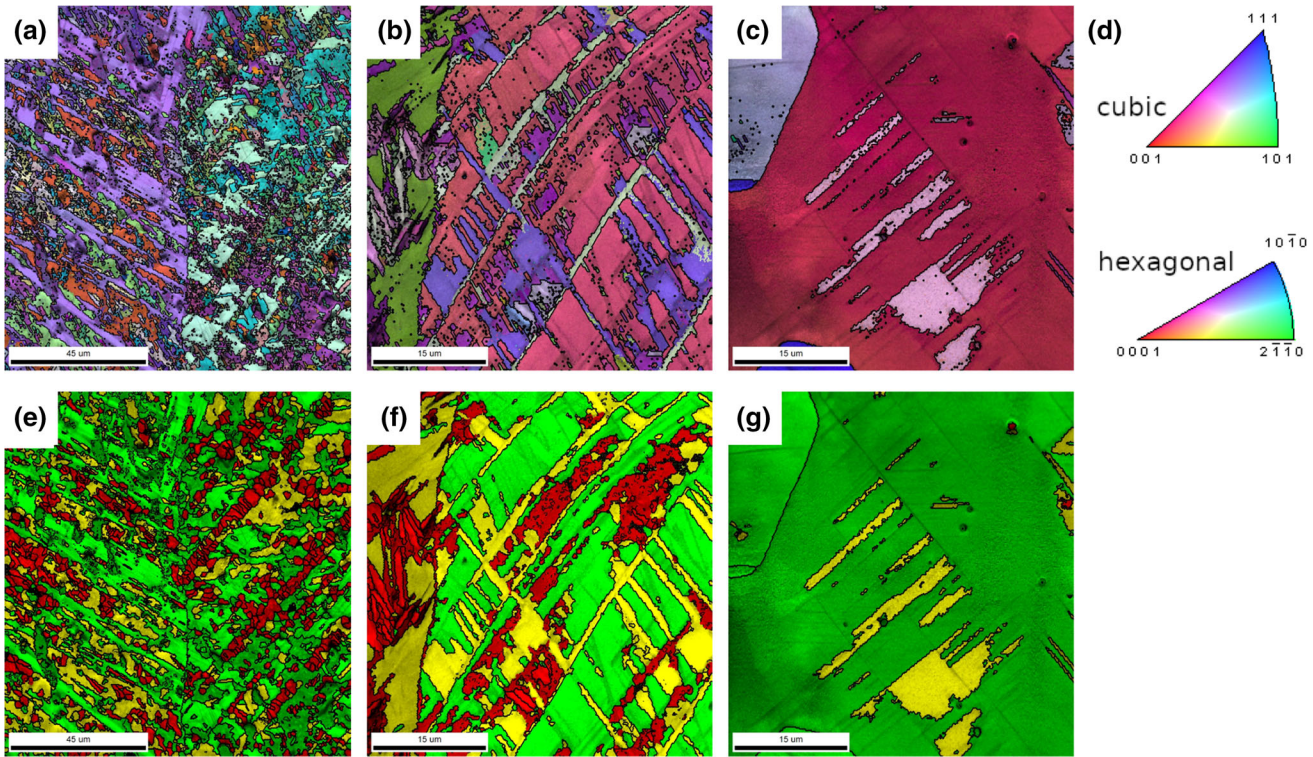
Fig. 7—(a to c) Inverse pole figure maps for A1, A6, and B11 samples, respectively. (d) Hexagonal and cubic ipf legend for (a) to (c). (e to g) Phase map for A1, A6, and B11 samples, respectively. In (e) to (g), green: austenite, yellow: ε-martensite, red: α′-martensite (Color figure online).

the arc and base metal. This makes the arc less effective on base metal, preventing melting and decreasing the dilution level. DuPont[42] showed this behavior for stainless steel welded by varying the volumetric filler metal feed rates and arc power. Although the material is different from the one studied here, the arc physics are the same.

The chemical compositions in this work (Table V) were in accordance with DuPont,[41,42] who stated that the dilution level obtained by geometric and chemical methods are linearly related because the manganese content increases with an increasing dilution level. Carbon does not present a significant change due to the similar filler and base metal carbon contents. However, the nickel content increases with decreasing dilution level. Both manganese and nickel are γ stabilizers and increase the γ phase field in the phase equilibrium diagram, as can be seen in Figure 3. Figures 3(a) through (c) show the decrease in the ferrite mass fraction for low temperatures. Figure 3(d) shows that with the addition of manganese and nickel, the temperature for which the structure is completely austenite reduces.

B. *Microstructure and Stacking Fault Energy*

De Cooman[53] already showed a phase diagram (wt pct C vs wt pct Mn) for the microstructure observed after quenching a high-manganese steel from 950°C to room temperature (Figure 10.5 at right, in the reference). This diagram enables the phase prediction for high-manganese steels when the steel is quenched from a high temperature. Based on the manganese and carbon composition, it is possible to know which phase will be present after the fast cooling from a high temperature. This diagram is very useful when the material is composed of a ternary system and the initial condition, *i.e.*, initial microstructure, grain size, and chemical composition, is similar to that used by De Cooman. According to Reference 53, A1 to A5 welds in this study present compositions that lie within the γ + ε + α′ phase field. The microstructures (Figures 5 and 7) for these samples showed agreement with De Cooman's diagram. However, A6 weld, which lies in the γ + ε phase field according to De Cooman's prediction, presents three phases (γ, ε and α′). Unlike the results shown by De Cooman, none of the welds in this work are ternary alloys. Therefore, the other elements may have changed the phase field extension, allowing compositions of 15.95 wt pct Mn and 0.12 wt pct C (A6 weld) to also have α′ martensite.

Looking at Figure 4, welding samples A1 to A5 presented negative SFE values, while positive values were found in A6-B11. This correlation is not a coincidence, as will be evidenced later. Hull and Bacon,[54] in their Dislocation in Face-centered Cubic Metals chapter, as well as Olson and Cohen,[27] have already stated that the energy associated with an SF comes from a sliding between {111} planes, forming a fault in the FCC stacking (ABCABCA) to a ABCA-BABC stacking, making an HCP stacking into the FCC structure. In the present study, the FCC phase is related

to the γ-austenite phase, while HCP corresponds to the ε-martensite phase. Xiong et al.[13] studied high-manganese steels with different Mn contents and they found SFE values from 2.9 to 28.5 mJ/m², showing γ + ε-martensite and γ + twins, respectively. Their results showed that the SFE values obtained by the thermodynamic model could be used to predict the phase formed in a state of non-equilibrium.

C. Microsegregation and Its Influence on the Microstructure

Since the structures formed by a solidification process can present microsegregation, this phenomenon was analyzed through map and spot chemical composition analysis using SEM-EDS. Figure 2 shows the iron and manganese map composition for a high and low dilution level welding sample. There are regions where Mn is in greater amounts and these manganese-rich areas are related to the last austenite to be formed from the liquid phase because the manganese content of the austenite increases as the temperature decreases. Therefore, α′-martensite regions correspond to the first austenite to form, which has less manganese. Figure 8 shows an austenite composition vs. temperature diagram for A1 weld, showing the phenomenon where nickel also presents this microsegregation behavior but at a level much lower than Mn. The same behavior was observed in the other welding samples.

In order to quantify and relate the microsegregation phenomenon with the SFE and also with De Cooman's diagram,[53] chemical analyses were done in both regions, where α′-martensite is present and where it is not. The results are shown in Figure 9. The colored background represents the manganese content, which forms a specific group according to Reference 53, while the triangular and square markers correspond to EDS measurements made in the γ + ε and α′ regions in the present study, respectively. Star markers correspond to Table V (EDS measurements made in a large area of the fusion zones). The results agreed with the prediction by Reference 53, where the γ + ε region presented a manganese content higher than 15 wt pct while the
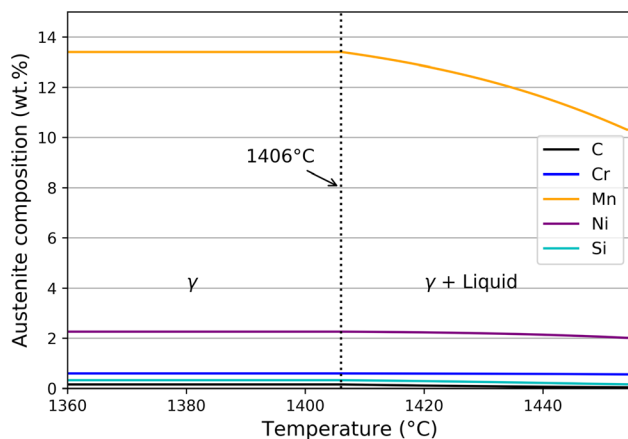
α′-martensite values were between 15 and 10 wt pct. Therefore, this result shows that microsegregation was responsible for the α′-martensite formation in A6 weld because regions with a manganese content lower than 15 wt pct present α′-martensite. The results showed that De Cooman's diagram is a good tool to predict the phase formation in high-manganese steels based on the C and Mn contents.

The SFE values were calculated from the chemical compositions shown in Figure 9 and from the chemical compositions of the rich and poor manganese regions for the B7-B11 welds. Negative SFE values obtained were related to α′-martensite, and the microsegregation phenomenon observed in this work also correlated to α′-martensite. Figure 10 shows that the first six welds
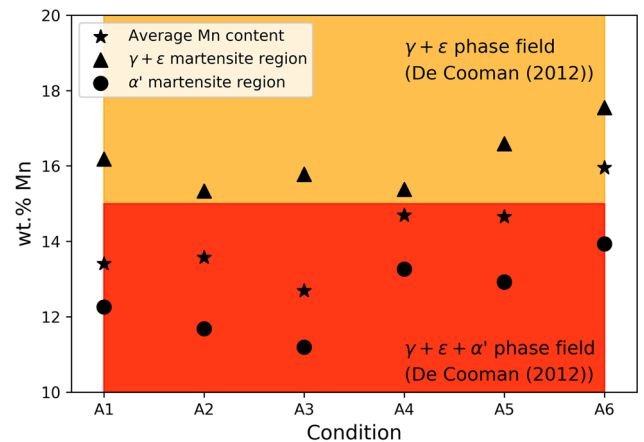

Fig. 9—Manganese content via EDS. Triangular markers correspond to EDS measures obtained from a large area of fusion zone, while the circles and star markers correspond to spot EDS measures in α′ and γ + ε phase region, respectively. The red and yellow areas in the graph refers to the manganese content in γ + ε + α′ and γ + ε phase region, respectively, obtained from Ref. [53] (Color figure online).

Fig. 8—Austenite composition in the γ and γ + Liquid phases field for A1 weld composition.
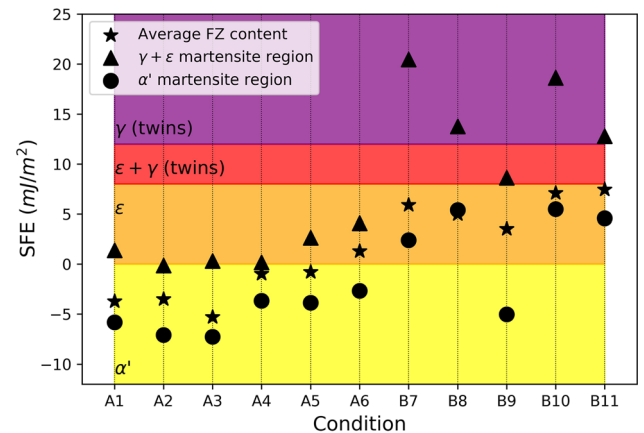

Fig. 10—Thermodynamic stacking fault energies. The markers correspond to calculus from the same markers in Fig. 9 and from the chemical compositions of the rich and poor manganese regions for the B7 to B11 welds. The color areas in the graph refer to SFE range and their microstructure prediction showed by Ref.[6]. Yellow: α′-martensite. Orange: ε-martensite: Red: ε-martensite + γ (twins). Purple: γ (twins) (Color figure online).

(A1-A6) presented negative SFE values in the α' region, while in a non-α' region, the SFE values were positive. Although the thermodynamic SFE should be used to analyze a $\gamma \rightarrow \epsilon$ phase transformation, SFE calculations were made in the α' phase region to estimate its value. Due to the $\gamma \rightarrow \alpha'$ diffusionless transformation, which maintains α' martensite with the same composition as prior austenite, the presence of α' martensite could be related to the SFE value. Figure 10 showed agreement with[53]; however, the phase diagram cannot give as much information about austenite mechanical instability as the SFE values can. At SFE values in the 12 to 40 mJ/m^2 range, the γ phase presents a tendency to form twins when subjected to a stress/strain.[22] With decreasing dilution levels, A1 $\rightarrow$ B11 welds in Figure 10, the austenite becomes more stable in almost all B$_i$ welding samples. The Mn-rich area is a region which forms twins instead of ϵ- or α'-martensite. However, even under these conditions, the microsegregation allows unstable γ regions, which could form ϵ by fast cooling from a high temperature or by a deformation process. These results show that thermodynamic SFE is a useful tool to predict the phases formed in high-manganese steels[6,7,13,51,53,55] and it can also predict the phase formation even with the microsegregation phenomenon due to a cast process in the fusion zone. Additionally, α' could also be predicted from a negative SFE value.

The importance of the microstructure and γ stability comes from the mechanical properties that each provides to the steel. Figure 6(a) shows that A1 weld does not have any phase transformation, which is demonstrated by the absence of a pop-in. From Figure 5, A1 weld presents few non-α'-martensite areas; therefore, the nanoindentations could have been done just in the α' phase, which can explain the low variation in elastic modulus and hardness values. On the other hand, A6 weld, which has a higher SFE and more non-α' regions, presented phase transformations in some measurements and not in others. The SFE value for this welding sample lies in $\gamma + \epsilon$ for manganese-rich areas, and in α' for Mn-poor areas. Phase transformations were not found in all measurements of B11 weld, which can indicate that in manganese-rich areas, the austenite was more stable and does not present phase transformations. These behaviors are strongly related to the mechanical properties, where increasing SFE values correlate to increasing toughness and ductility due to the austenite becoming more stable and preventing martensite formation.[6,7] Welding samples A6 and B11, which do not show α' or only show it in small quantities, presented low hardness compared with A1, which showed a high amount of α'-martensite. Additionally, Young's modulus decreases with increasing SFE values, or with increasing austenite stability. This can provide higher ductility and toughness with high strength, because fragile phases, such as α'- and ϵ-martensite, are not formed during the stress/strain process.

If the dilution level can provide a good idea of the SFE value in the fusion zone and if it can be used to predict the microstructure and/or austenite stability in high-manganese steels, then knowledge of the base and filler metal chemical compositions can be used to predict

the microstructure desired from a dilution level chosen. Figure 11 shows the SFE and the Total, Chemical and Magnetic Gibbs free energy components from some dilution levels for various base metal steels. Additionally, the measurements that were made in this work using SAE 1012 steel are marked as black triangles.

Both total and chemical free energy curves present similar behavior for all steels, as can be seen in Figures 11(b) and (c). On the other hand, the magnetic component decrease for almost all alloys. Just commercial high-Mn steel presents an increase in the magnetic component (Figure 11(d)), where it is the only steel with a manganese content higher than the filler metal used. Furthermore, for all other alloys, the magnetic component presents a lower effect on the total Gibbs free energy, decreasing at a greater rate until 40 pct in dilution.

The chemical compositions for all steels used as base metal are presented in Table VI. Depending on the base metal, it is possible to achieve different microstructures, as Figure 11(a) shows, and this can result in different mechanical properties, as was found in the present study by nanoindentation measurements. In addition to using this relationship for different base metals, it can also be used for the mixture between different electrodes, where one must have a high-manganese steel filler metal. Then, different alloys can be used for different weld situations where the properties and austenite behaviors must be controlled. The results showed that thermodynamic SFE, in addition to the ϵ and twins prediction, can give an idea of whether α' will form in high-manganese steel.

V. CONCLUSIONS

An SFE, phase transformation, and dilution level relationship was studied in welds made from a high-manganese steel filler metal (21 wt pct Mn) and a base metal steel with 0.6 wt pct Mn with dilution levels in a 7-41 pct range.

De Cooman's non-equilibrium diagram for high-manganese steels was shown to be a good tool to predict the microstructure in these steels. The microstructure could not be explained by the diagram when the microsegregation due to the welding process created regions with manganese content that could potentially form α'-martensite.

Thermodynamic SFE values could predict the formation of different phases, including α'-martensite. Negative SFE values were related to α' regions, while positive SFE was obtained in $\gamma + \epsilon$ areas. SFE calculations in each region, with high or low manganese content, showed that negative SFE values were found in those regions where α' was observed, while positive SFE values were obtained in those where α' was not observed, which leads to the conclusion that thermodynamic SFE can be used to give an idea whether α'-martensite will form or not.

Nanoindentation measurements showed that γ presented a phase transformation when subjected to stress/strain in the samples with SFE values in the range of $\gamma + \epsilon$-martensite prediction. However, none phase
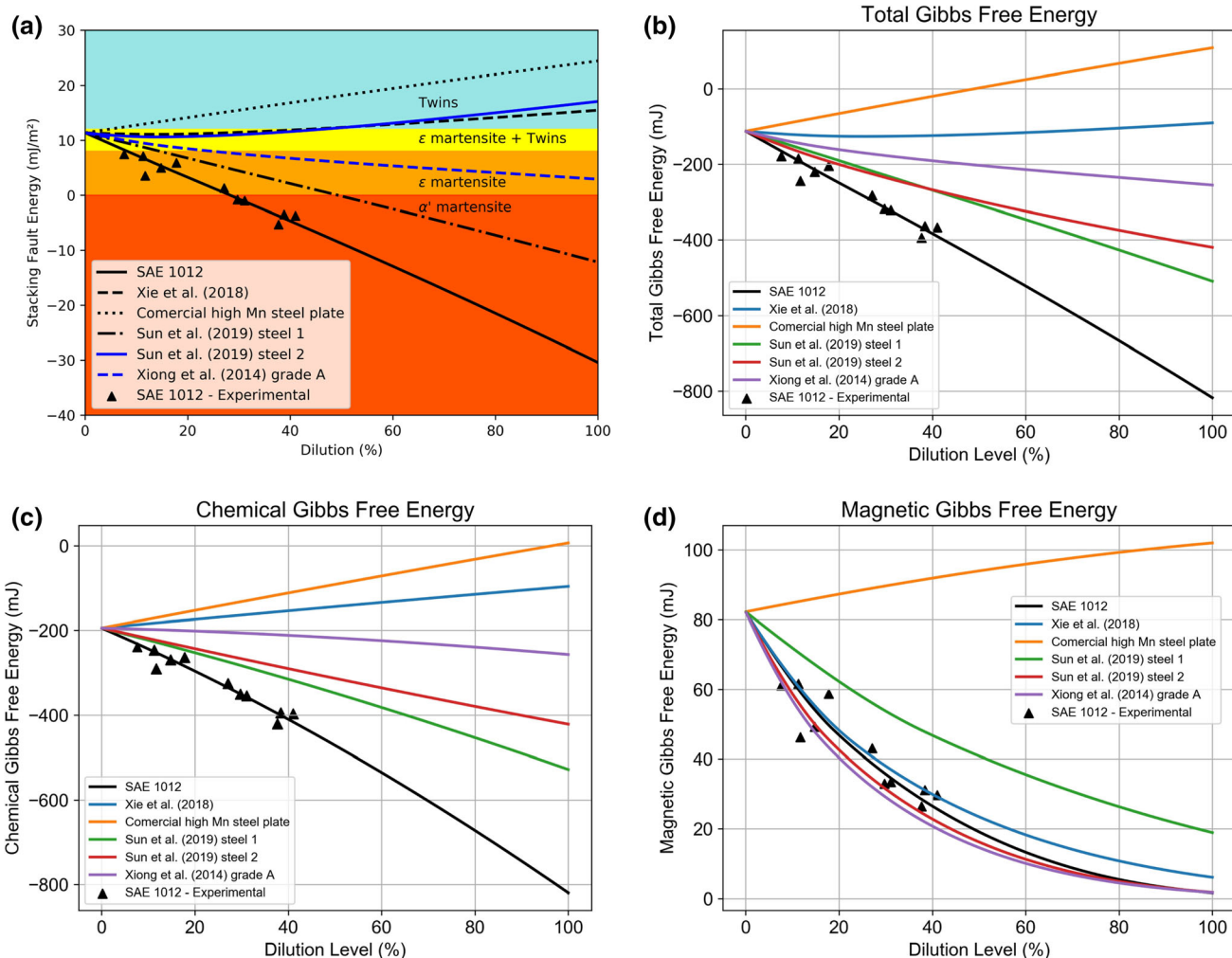
Fig. 11—Dilution level *vs* (*a*) SFE, (*b*) total Gibbs free energy, (*c*) chemical Gibbs free energy, and (*d*) magnetic Gibbs free energy for various base metal steels. The colors in the background refer to the phase present due to an austenite decomposition for some SFE values. Red: α′-martensite. Orange: ε-martensite. Yellow: ε + γ + *twins*. Cian: γ + *twins* according to Ref. [6] (Color figure online).

Table VI. Chemical Compositions for all Materials Presented in Fig. 11

Base Metal	Mn	C	Si	Al	Cr	Ni	Fe	Ref.
Commercial High-Mn steel	26.1	0.44	0.04	—	3.24	0.02	bal.	
Xie *et al.* (2018)	17.74	0.57	2.96	0.44	—	—	bal.	56
Sun *et al.* (2019) steel 1	10.4	0.2	—	—	—	—	bal.	57
Sun *et al.* (2019) steel 2	9.7	0.2	3.4	3.2	—	—	bal.	57
Xiong *et al.* (2014)	17.30	0.32	5.71	—	—	—	bal.	13
SAE 1012 Steel	0.6	0.12	—	—	—	—	bal.	

transformations were found for those samples that lay in the γ + twins SFE range. These transformations were noted for some measurements with medium and low dilution levels, while for those with high dilution levels, a transformation was not found since the measurements were taken from the α′ martensite phase. The hardness and Young's modulus agreed with this assumption because they showed high hardness and elastic modulus for high dilution levels, which is an α′ martensite feature.

The results showed that the dilution level/SFE relationship can be used to predict the microstructure of high-manganese steels obtained by welding. Additionally, a relationship between negative SFE and the α′ martensite presence was observed in the present study. Although thermodynamic SFE is not used for α′-martensite prediction in high-manganese steels, it was found that a negative SFE value is correlated with the presence of α′-martensite even in microsegregation regions.

ACKNOWLEDGMENTS

CONFLICT OF INTEREST

The authors declare that they have no conflicts of interest.

REFERENCES

1. W. Yan, L. Fang, K. Sun, and Y. Xu: *Mater. Sci. Eng. A*, 2007, vols. 460–461, pp. 542–49, https://doi.org/10.1016/j.msea.2007.02.094.
2. B.D. Shanina, V.G. Gavriljuk, H. Berns, and F. Schmalt: *Steel Res.*, 2002, vol. 73 (3), pp. 105–13, https://doi.org/10.1002/srin.200200181.
3. T.H. Lee, C.S. Oh, and S.J. Kim: *Scripta Mater.*, 2008, vol. 58 (2), pp. 110–13, https://doi.org/10.1016/j.scriptamat.2007.09.029.
4. S. Lee, J. Kim, S.J. Lee, and B.C. De Cooman: *Scripta Mater.*, 2011, vol. 65 (12), pp. 1073–76, https://doi.org/10.1016/j.scriptamat.2011.09.019.
5. O. Bouaziz, S. Allain, and C. Scott: *Scripta Mater.*, 2008, vol. 58 (6), pp. 484–87, https://doi.org/10.1016/j.scriptamat.2007.10.050.
6. B. De Cooman: in *Automotive Steels* (Elsevier, 2017), pp. 317–85. https://doi.org/10.1016/B978-0-08-100638-2.00011-0.
7. S. Curtze and V.T. Kuokkala: *Acta Mater.*, 2010, vol. 58 (15), pp. 5129–141, https://doi.org/10.1016/j.actamat.2010.05.049.
8. B.C. De Cooman, O. Kwon, and K.G. Chin: *Mater. Sci. Technol.*, 2012, vol. 28 (5), pp. 513–27, https://doi.org/10.1179/1743284711Y.0000000095.
9. O. Bouaziz, S. Allain, C. Scott, P. Cugy, and D. Barbier: *Curr. Opin. Solid State Mater. Sci.*, 2011, vol. 15 (4), pp. 141–68, https://doi.org/10.1016/j.cossms.2011.04.002.
10. M. Toloui and M. Militzer: *Acta Mater.*, 2018, vol. 144, pp. 786–800, https://doi.org/10.1016/j.actamat.2017.11.047.
11. C.. Liu, Q. Peng, Z. Xue, S. Wang, and C. Yang: *Materials*, 2018, vol. 11 (11), p. 2242, https://doi.org/10.3390/ma11112242.
12. Z.L. Li, D. Chen, J. Kang, G. Yuan, and G.D. Wang: *Steel Res. Int.*, 2018, vol. 89 (5), p. 1700484, https://doi.org/10.1002/srin.201700484.
13. R. Xiong, H. Peng, H. Si, W. Zhang, and Y. Wen: *Mater. Sci. Eng. A*, 2014, vol. 598, pp. 376–86, https://doi.org/10.1016/j.msea.2014.01.046.
14. S. Curtze, V.T. Kuokkala, A. Oikari, J. Talonen, and H. Hänninen: *Acta Mater.*, 2011, vol. 59 (3), pp. 1068–76, https://doi.org/10.1016/j.actamat.2010.10.037.
15. H.M. Otte: *Acta Metall.*, 1957, vol. 5 (11), pp. 614–27, https://doi.org/10.1016/0001-6160(57)90108-6.
16. R.E. Smallman and K.H. Westmacott: *Philos. Mag.*, 1957, vol. 2 (17), pp. 669–83, https://doi.org/10.1080/14786435708242709.
17. P.J. Ferreira and P. Müllner: *Acta Mater.*, 1998, vol. 46 (13), pp. 4479–84, https://doi.org/10.1016/S1359-6454(98)00155-4.
18. J.N. Israelachvili and D. Tabor: *Proc. R. Soc. Lond. Ser. A*, 1959, vol. 249 (1256), pp. 114–37, https://doi.org/10.1098/rspa.1959.0011.
19. S. Zhao, G.M. Stocks, and Y. Zhang: *Acta Mater.*, 2017, vol. 134, pp. 334–45, https://doi.org/10.1016/j.actamat.2017.05.001.
20. R. Xie, W. Li, S. Lu, Y. Song, and L. Vitos: *J. Phys.*, 2019, vol. 31 (6), p. 065703, https://doi.org/10.1088/1361-648X/aaf2fa.
21. S. Allain, J.P. Chateau, O. Bouaziz, S. Migot, and N. Guelton: *Mater. Sci. Eng. A*, 2004, vols. 387–389 (1–2 SPEC. ISS.), pp. 158–62, https://doi.org/10.1016/j.msea.2004.01.059.
22. L. Remy and A. Pineau: *Mater. Sci. Eng.*, 1977, vol. 28 (1), pp. 99–107, https://doi.org/10.1016/0025-5416(77)90093-3.
23. T.H. Lee, E. Shin, C.S. Oh, H.Y. Ha, and S.J. Kim: *Acta Mater.*, 2010, vol. 58 (8), pp. 3173–86, https://doi.org/10.1016/j.actamat.2010.01.056.
24. T. Maki: *Mater. Sci. Forum*, 1991, vols. 56–58, pp. 157–68, https://doi.org/10.4028/www.scientific.net/MSF.56-58.157.
25. J.K. Hwang: *J. Mater. Sci.*, 2020, vol. 55 (4), pp. 1779–95, https://doi.org/10.1007/s10853-019-04018-1.
26. D. Pierce, J. Jiménez, J. Bentley, D. Raabe, and J. Wittig: *Acta Mater.*, 2015, vol. 100, pp. 178–90, https://doi.org/10.1016/j.actamat.2015.08.030.
27. G.B. Olson and M. Cohen: *Metall. Trans. A*, 1976, vol. 7 (12), pp. 1897–1904, https://doi.org/10.1007/BF02659822.
28. K. Ishida: *Physica Status Solidi A*, 1976, vol. 36 (2), pp. 717–28, https://doi.org/10.1002/pssa.2210360233.
29. A.T. Dinsdale: *Calphad*, 1991, vol. 15 (4), p. 317, https://doi.org/10.1016/0364-5916(91)90030-N.
30. O. Redlich and A.T. Kister: *Ind. Eng. Chem.*, 1948, vol. 40 (2), pp. 345–48, https://doi.org/10.1021/ie50458a036.
31. S. Cotes, M. Sade, and A.F.. Guillermet: *Metall. Mater. Trans. A*, 1995, vol. 26A (8), pp. 1957–69, https://doi.org/10.1007/BF02670667.
32. A. Dumay, J.P. Chateau, S. Allain, S. Migot, and O. Bouaziz: *Mater. Sci. Eng. A*, 2008, vols. 483–484 (1–2 C), pp. 184–87, https://doi.org/10.1016/j.msea.2006.12.170.
33. K. Ishida and T. Nishizawa: *Trans. Jpn. Inst. Met.*, 1974, vol. 15 (3), pp. 225–31, https://doi.org/10.2320/matertrans1960.15.225.
34. W.S. Yang and C.M. Wan: *J. Mater. Sci.*, 1990, vol. 25 (3), p. 1821, https://doi.org/10.1007/BF01045392.
35. S.. Chen, C.Y. Chung, C. Yan, and T.Y. Hsu: *Mater. Sci. Eng. A*, 1999, vol. 264 (1–2), pp. 262–68, https://doi.org/10.1016/s0921-5093(98)01105-8.
36. P.H. Adler, G.B. Olson, and W.S. Owen: *Metall. Mater. Trans. A*, 1986, vol. 17A (10), pp. 1725–37, https://doi.org/10.1007/BF02817271.
37. I.A. Yakubtsov, A. Ariapour, and D.D. Perovic: *Acta Mater.*, 1999, vol. 47 (4), pp. 1271–79, https://doi.org/10.1016/S1359-6454(98)00419-4.
38. G. Inden: *Physica B+C*, 1981, vol. 103 (1), pp. 82–100.
39. X. Wu and T.Y. Hsu: *Mater. Charact.*, 2000, vol. 45 (2), pp. 137–42, https://doi.org/10.1016/S1044-5803(00)00066-8.
40. Y.S. Zhang, X. Lu, X. Tian, and Z. Qin: *Mater. Sci. Eng. A*, 2002, vol. 334 (1–2), pp. 19–27, https://doi.org/10.1016/S0921-5093(01)01781-6.
41. J.N. DuPont and A.R. Marder: *Metall. Mater. Trans. B*, 1996, vol. 27B (3), pp. 481–89, https://doi.org/10.1007/BF02914913.
42. J.N. Dupont: in *Welding Fundamentals and Processes*, vol. 6A (ASM International, 2018), pp. 115–121. https://doi.org/10.31399/asm.hb.v06a.a0005589.
43. G.M. Pharr: *J. Mater. Res.*, 1992, vol. 7 (6), pp. 1564–83, https://doi.org/10.1557/JMR.1992.1564.
44. R. Elliott, K. Coley, S. Mostaghel, and M. Barati: *Jom*, 2018, vol. 70 (5), pp. 680–90, https://doi.org/10.1007/s11837-018-2773-8.
45. B. Hu, B. Luo, F. Yang, and H. Dong: *J. Mater. Sci. Technol.*, 2017, vol. 33 (12), pp. 1457–64, https://doi.org/10.1016/j.jmst.2017.06.017.
46. X. Qiao, L. Han, W. Zhang, and J. Gu: *Mater. Charact.*, 2015, vol. 110, pp. 86–93, https://doi.org/10.1016/j.matchar.2015.10.024.
47. S. Sadeghpour, A. Kermanpur, and A. Najafizadeh: *Mater. Sci. Eng. A*, 2014, vol. 612, pp. 214–16, https://doi.org/10.1016/j.msea.2014.06.055.
48. Y. Kim, T.H. Ahn, D.W. Suh, and H.N. Han: *Scripta Mater.*, 2015, vol. 104, pp. 13–16, https://doi.org/10.1016/j.scriptamat.2015.03.014.
49. T.H. Ahn, S.B. Lee, K.T. Park, K.H. Oh, and H.N. Han: *Mater. Sci. Eng. A*, 2014, vol. 598, pp. 56–61, https://doi.org/10.1016/j.msea.2014.01.030.
50. T.H. Ahn, C.S. Oh, D.H. Kim, K.H. Oh, H.. Bei, E.P. George, and H.N. Han: *Scripta Mater.*, 2010, vol. 63 (5), pp. 540–43, https://doi.org/10.1016/j.scriptamat.2010.05.024.
51. B.C. De Cooman, Y. Estrin, and S.K. Kim: *Acta Mater.*, 2018, vol. 142, pp. 283–362, https://doi.org/10.1016/j.actamat.2017.06.046.

52. C. Haase, C. Zehnder, T. Ingendahl, A. Bikar, F. Tang, B. Hallstedt, W. Hu, W. Bleck, and D.A. Molodov: *Acta Mater.*, 2017, vol. 122, pp. 332–43, https://doi.org/10.1016/j.actamat.2016.10.006.

53. B. De Cooman: in *Phase Transformations in Steels*, vol. 2 (Elsevier, 2012), pp. 295–331. https://doi.org/10.1533/9780857096111.2.295.

54. D. Hull, D.J. Bacon: Introduction to Dislocations (Elsevier, 2011). https://doi.org/10.1016/C2009-0-64358-0.

55. R. Xiong, H. Peng, S. Wang, H. Si, and Y. Wen: *Mater. Des.*, 2015, vol. 85, pp. 707–14, https://doi.org/10.1016/j.matdes.2015.07.072.

56. Q. Xie, Z. Pei, J. Liang, D. Yu, Z. Zhao, P.. Yang, R. Li, M. Eisenbach, and K. An: *Acta Mater.*, 2018, vol. 161, pp. 273–84, https://doi.org/10.1016/j.actamat.2018.09.020.

57. B. Sun, D. Palanisamy, D. Ponge, B. Gault, F. Fazeli, C.. Scott, S. Yue, and D. Raabe: *Acta Mater.*, 2019, vol. 164, pp. 683–96, https://doi.org/10.1016/j.actamat.2018.11.029.